antioxidants

MDPI

Article

Acute Influenza A Infection Reveals Distinct Bone and Skeletal Muscle Responses in Cigarette Smoke–Exposed Male Mice

Stanley M. H. Chan, Kevin Mou, Simone N. De Luca, Hao Wang, Stavros Selemidis, Steven Bozinovski and Ross Vlahos *

Centre for Respiratory Science and Health, School of Health and Biomedical Sciences, STEM College, RMIT University, Bundoora, VIC 3083, Australia; kevin.mou@rmit.edu.au (K.M.); hao.wang@rmit.edu.au (H.W.)
* Correspondence: ross.vlahos@rmit.edu.au; Tel: +61–3–9925–7362

Abstract

Musculoskeletal disorders are prevalent extrapulmonary comorbidities of chronic obstructive pulmonary disease, encompassing skeletal muscle dysfunction and compromised bone microarchitecture. However, the relative contributions of cigarette smoke (CS) exposure and acute viral exacerbation to muscle and bone pathology remain incompletely defined. Using male BALB/c mice exposed to CS for 8 weeks followed by influenza A virus (IAV) infection to model viral acute exacerbation of chronic obstructive pulmonary disease (COPD), we assessed airway inflammation, tibial bone microarchitecture, hindlimb muscle mass, tibialis anterior (TA) contractile function, myofiber morphology, BA–F8–positive fiber proportion, oxidative protein modification, and calcium–handling protein expression, with parallel assessment of ebselen–associated differences in skeletal muscle outcomes. CS exposure and IAV infection induced robust airway inflammation, with the combined CS + IAV group showing the greatest inflammatory burden. In the eight–week vehicle–treated cohort, CS exposure was associated with a 57% reduction in bone volume fraction (BV/TV) and approximately 46% greater trabecular separation relative to Sham Veh PBS controls. Complementary analyses of independent chronic CS cohorts identified reduced expression of the osteogenic matrix genes Ibsp, Spp1, and Bglap and altered trabecular microarchitecture. In Sham mice, acute IAV infection was associated with a 38% reduction in BV/TV, indicating a rapid trabecular response to respiratory viral challenge. In skeletal muscle, CS exposure reduced selected hindlimb muscle masses and was associated with a lower BA–F8–positive fiber proportion. Mouse–level mean myofiber cross–sectional area (CSA) and pooled fiber–size distributions indicated smaller myofibers and a shift toward lower CSA values in CS–exposed vehicle–treated groups, whereas IAV infection alone had limited effects on muscle mass or fiber–type composition. However, IAV challenge superimposed on CS exposure produced the greatest TA force deficit, despite limited evidence of additional muscle mass loss, and was accompanied by treatment–dependent patterns of sarco/endoplasmic reticulum Ca^{2+}–ATPase 2 (SERCA2) and stromal interaction molecule 1 (STIM1) abundance. Ebselen–related interactions were detected for contractile outcomes, mean myofiber CSA, and BA–F8–positive fiber proportion, whereas combined analysis of protein carbonylation did not detect significant main effects or interactions. These findings indicate that CS exposure and acute IAV infection exert distinct but intersecting effects on bone and skeletal muscle, identifying trabecular bone as an acutely responsive compartment following respiratory viral infection and highlighting a dissociation between muscle quantity and contractile function during viral exacerbation.

Academic Editor: Niki L. Reynaert

Received: 3 September 2026
Revised: 10 November 2026
Accepted: 13 November 2026
Published: 23 November 2026

Copyright: © 2026 by the authors. Licensee MDPI, Basel, Switzerland. This article is an open access article distributed under the terms and conditions of the Creative Commons Attribution (CC BY) license.

Keywords: AECOPD; ebselen; muscle weakness; skeletal fragility; micro−computed tomography

1. Introduction

Chronic obstructive pulmonary disease (COPD) is a progressive inflammatory lung disease characterized by persistent airflow limitation and chronic respiratory symptoms, most commonly associated with cigarette smoke (CS) exposure [1,2]. Although COPD is primarily defined by respiratory pathology, it is increasingly recognized as a systemic disease with clinically important extrapulmonary manifestations, including skeletal muscle dysfunction and osteoporosis [3–5]. These musculoskeletal comorbidities substantially impair exercise tolerance, mobility, and quality of life and are associated with increased risk of hospitalization and mortality [6–8]. Importantly, muscle and bone dysfunction frequently coexist in COPD, suggesting that shared disease cues such as systemic inflammation, physical inactivity, altered body composition, oxidative stress, and disrupted muscle–bone crosstalk may contribute to the development of these comorbidities [9,10].

Acute exacerbations of COPD (AECOPD) represent episodes of acute worsening of respiratory symptoms and are major drivers of disease progression, hospitalization, and mortality [11]. Infectious triggers account for a substantial proportion of exacerbations, with respiratory viruses commonly detected during AECOPD [11,12]. Among these, influenza A virus (IAV) is clinically relevant because influenza infection can precipitate acute respiratory deterioration, amplify airway inflammation, and worsen outcomes in patients with COPD [13,14]. IAV therefore provides a useful experimental trigger to model virus−induced AECOPD on a CS−exposed background. In support of this approach, previous preclinical work from our group showed that IAV infection exacerbated CS−induced airway inflammation and worsened tibialis anterior (TA) force−generating capacity, despite limited additional effects on muscle mass [6]. These observations raise the possibility that viral exacerbation may impair muscle function through mechanisms that are not fully explained by muscle wasting alone [15].

Oxidative stress is a central biological feature of COPD and is further amplified during exacerbations, arising from cigarette−smoke−derived oxidants, activated inflammatory cells, mitochondrial dysfunction, and impaired antioxidant defenses [16,17]. Excessive reactive oxygen species can promote airway inflammation and tissue injury but may also propagate systemic effects beyond the lung [17]. In skeletal muscle, oxidative stress has been implicated in myofiber atrophy, altered fiber−type composition, impaired mitochondrial function, disrupted proteostasis, and reduced contractile performance [3,5]. In bone, oxidative stress and inflammation can suppress osteoblast function, promote osteoclastogenesis, and impair bone remodeling, thereby contributing to loss of bone mass and microarchitectural integrity [10,18–21]. Thus, redox imbalance may represent a shared mechanism linking respiratory inflammation with musculoskeletal deterioration during COPD and AECOPD.

Despite this, the relative contribution of chronic CS exposure and acute viral exacerbation to bone and skeletal muscle pathology remains incompletely understood [9,10]. In particular, it is unclear whether acute IAV infection independently impairs bone microarchitecture, whether IAV exacerbates CS−exposure−induced skeletal muscle wasting or primarily affects muscle function, and whether skeletal muscle outcomes differ with ebselen treatment administered during the CS exposure protocol. This distinction is important because skeletal muscle mass, muscle function, and bone structure may respond differently to chronic and acute respiratory insults [9]. Moreover, understanding

whether oxidative stress contributes to these divergent musculoskeletal outcomes may identify therapeutic opportunities for limiting systemic comorbidities during COPD exacerbations.

Ebselen is a glutathione peroxidase mimetic with antioxidant and anti−inflammatory properties that has previously been shown to attenuate oxidant−dependent pathology in experimental models relevant to COPD [22,23]. As oxidative stress is strongly implicated in COPD−associated skeletal muscle dysfunction [10,17,24,25], ebselen provides a useful pharmacological approach to investigate the potential involvement of redox−associated processes in CS−exposure− and IAV−infection−induced musculoskeletal pathology. In the present study, we used a mouse model of chronic CS exposure followed by acute IAV infection to determine whether respiratory viral exacerbation differentially affects bone microarchitecture and skeletal muscle structure and function. Bone outcomes were assessed as changes in tibial microarchitecture; the acute three−day post−infection assessment was not intended to establish the development of osteoporosis. We further used ebselen, a glutathione peroxidase mimetic with antioxidant and anti−inflammatory properties, to examine whether the associated skeletal muscle abnormalities were modified in ebselen−treated mice. We hypothesized that acute IAV infection and chronic CS exposure would produce distinct but intersecting musculoskeletal phenotypes, with rapid effects on trabecular bone and altered skeletal muscle function on a CS−exposed background, with skeletal muscle outcomes differing according to ebselen treatment. Building on our previous characterization of the CS/IAV model [6], the present study adds tibial microarchitectural outcomes and SERCA2/STIM1 measurements and evaluates ebselen−associated differences in skeletal muscle endpoints using combined factorial analyses.

2. Materials and Methods

2.1. Animals and Housing

Seven−week−old male BALB/c mice were obtained from the Animal Resources Centre (Perth, WA, Australia) and acclimatized for one week at the RMIT Animal Facility (Bundoora, VIC, Australia). Male mice were used to maintain consistency with our established CS/IAV experimental model and enable comparison with previous studies using this protocol [6,22,26]. Mice were housed in micro−isolator cages at 21 °C under a 12:12 h light/dark cycle (lights on 07:00), with chow and water provided ad libitum. Body weight was monitored three times per week. All procedures were conducted in accordance with the Australian Code for the Care and Use of Animals for Scientific Purposes and were approved by the RMIT University Animal Ethics Committee under protocols AEC 1533 (approved project period commencing 11 January 2016) and AEC 1929 (approved 10 December 2019; approved project period commencing 6 January 2020).

2.2. Animal Care and Monitoring

Mice were monitored daily throughout the study, with increased monitoring following IAV inoculation. Animals were assessed for body weight loss, posture, activity, grooming behavior, and respiratory distress. Humane endpoint criteria included severe respiratory distress, inability to access food or water, or continued weight loss exceeding predetermined ethical limits. No animals reached humane endpoint criteria and no unexpected adverse events occurred.

2.3. Study Design and Sample Size

Mice were assigned to eight experimental groups according to room−air or cigarette smoke exposure, phosphate−buffered saline (PBS) or IAV inoculation, and vehicle or ebselen treatment. The individual mouse was the experimental unit. Animals were allocated to experimental groups using their animal identification numbers, with consideration of baseline body weight to achieve comparable starting body weights among groups. No formal randomization sequence was used. Animals from the different experimental groups were distributed across cages and experimental runs to minimize potential cage, exposure chamber, and batch effects. No formal a priori sample−size calculation was performed. Group sizes were based on previous studies using this established cigarette smoke and influenza A virus model, together with experimental feasibility and tissue availability [6,22,26]. Fourteen mice were allocated to each experimental group. Body weight was monitored in all 14 mice throughout the experimental period. At the scheduled endpoint, mice and available tissues were allocated across different outcome measurements according to the experimental design and tissue requirements of each assay. Eight mice per group contributed to bronchoalveolar lavage fluid (BALF) and, where applicable, micro−CT analyses, while six mice per group contributed to muscle mass, TA contractile function, locomotor activity, body−composition, immunohistology, OxyBlot, and Western Blot analyses. These analysis−specific group sizes reflect the allocation of animals and tissues across different endpoint measurements and do not represent animal attrition or exclusion based on the observed results. The number of animals contributing to each outcome is reported in the corresponding figure legend and Supplementary Table S1. Vehicle− and ebselen−treated groups were studied concurrently. Vehicle−treated animals and tissues also contributed to our previous study [6]; relevant measurements were recounted or reanalyzed for the present study, while the ebselen−treated groups are reported here for the first time. The present investigation used a separate animal cohort from that reported in [22]. Although both studies assessed BALF inflammatory cellularity using closely related CS/IAV protocols, the BALF measurements reported here were obtained independently of the dataset in [22].

2.4. Inclusion and Exclusion Criteria

Animals were included in the study if they completed the assigned exposure and treatment protocol and reached the scheduled experimental endpoint. All 14 mice allocated to each experimental group completed the study and contributed to body−weight monitoring. Subsets of mice and available tissues were allocated to different endpoint measurements according to the experimental design and tissue requirements of each assay. These analysis−specific subsets were not selected on the basis of the magnitude, direction, or statistical significance of the observed results. Outcome data were excluded only where an assay failed to produce data of sufficient technical quality for analysis. No outcome data were excluded for technical reasons. Exact sample sizes are reported in the corresponding figure legends and Supplementary Table S1.

2.5. Blinding

Personnel conducting cigarette smoke exposure, IAV inoculation, and ebselen administration were aware of group allocation because of the nature of the interventions. Samples were identified using animal identification numbers throughout data collection and analysis. Group allocation was visible during outcome assessment and statistical analysis; therefore, these procedures were not formally blinded.

2.6. Outcome Measures

Primary outcome measures included tibialis anterior contractile function, trabecular bone microarchitecture, and airway inflammatory cell counts. Secondary outcome measures included skeletal muscle mass, locomotor activity, BA−F8−positive fiber proportion, OxyBlot signal, SERCA2 expression, STIM1 expression, and bone−related gene expression.

2.7. Cigarette Smoke Exposure and Ebselen Administration

Mice were assigned to eight experimental groups comprising CS exposure or room air (Sham), inoculation with influenza A virus (IAV) or PBS diluent, and treatment with ebselen or vehicle (Sham Veh PBS, Sham Veh IAV, Sham Ebs PBS, Sham Ebs IAV, CS Veh PBS, CS Veh IAV, CS Ebs PBS, CS Ebs IAV). Mice were exposed to room air (Sham) or CS for 8 weeks and subsequently inoculated intranasally with IAV to model a viral acute exacerbation or PBS diluent as vehicle control (Figure 1A,B). CS exposure was performed using 18 L Perspex chambers within a standard fume hood. Smoke was generated from Winfield Red cigarettes (total particulate matter of 419 mg·m^{-3} with ≤16 mg tar, ≤1.2 mg nicotine, ≤15 mg carbon monoxide; Philip Morris, Sydney, Australia). This level of CS exposure causes increases in blood carboxyhemoglobin comparable to that observed in human smokers [27,28]. Mice were exposed to smoke from three cigarettes over a 1 −h period; smoke was generated over ~10 s in 60 mL tidal volumes to mimic inhalation rates. Exposures were conducted three times per day with a 2 −h break between sessions (nine cigarettes/day total), five days/week, for eight weeks. Sham controls were placed in identical chambers with room air as previously described [6,29]. Ebselen (10 mg·kg^{-1}; Sigma Aldrich, Meolbourne, Australia) was prepared by dissolving in 5% carboxymethyl−cellulose (CM−cellulose) in PBS and administered via oral gavage once daily, at least 1 h prior to the first cigarette smoke exposure. Vehicle−treated mice received 5% CM−cellulose in PBS.

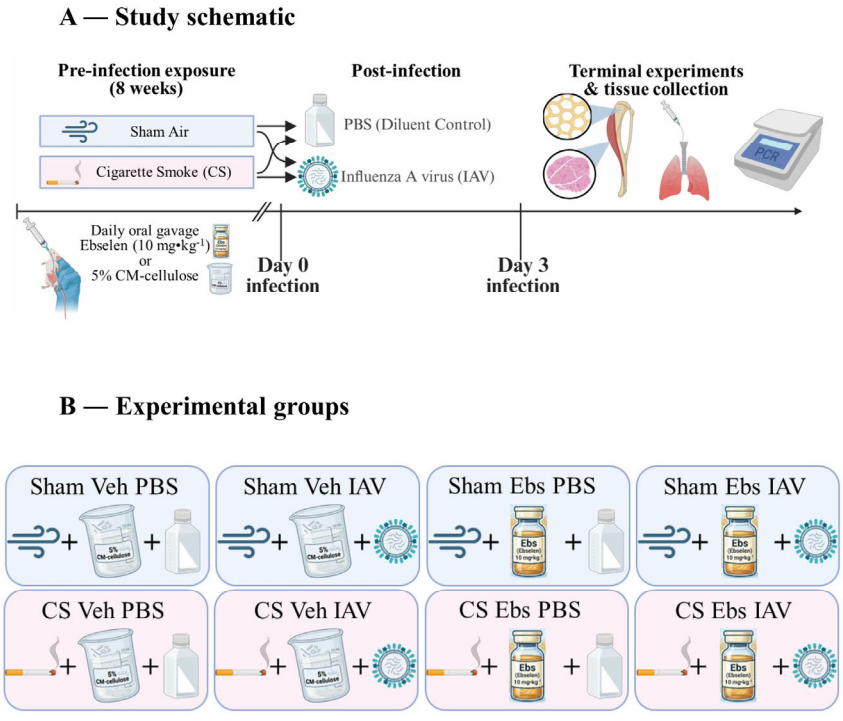

Figure 1. Experimental design and treatment groups. (**A**) Schematic overview of the experimental protocol. Mice were exposed to room air (Sham) or cigarette smoke (CS) for 8 weeks, with daily oral

gavage of either vehicle or ebselen (10 mg·kg^{-1}). At day 0, mice were intranasally inoculated with phosphate−buffered saline (PBS; diluent control) or influenza A virus (IAV) to model acute viral exacerbation on a CS−exposed background. Terminal experiments and tissue collection were performed at day 3 post−infection, including bronchoalveolar lavage fluid collection, tibial bone assessment, hindlimb muscle analyses, TA contractile testing, and molecular assays. (**B**) Experimental groups included Sham Veh PBS, Sham Veh IAV, Sham Ebs PBS, Sham Ebs IAV, CS Veh PBS, CS Veh IAV, CS Ebs PBS, and CS Ebs IAV. Veh, vehicle; Ebs, ebselen; PBS, phosphate−buffered saline.

2.8. Influenza A Virus Infection

Following 8 weeks of CS exposure, mice were anesthetised with isoflurane in a class II biosafety cabinet and inoculated intranasally with influenza A virus (Mem71 strain; 1 × $10^{4.5}$ plaque−forming units) in PBS, or PBS alone (diluent control), to model a clinically relevant, virus−triggered acute exacerbation on a cigarette smoke background (AECOPD) [6,22], noting that respiratory viruses are detected in a substantial proportion of COPD exacerbations and influenza is among the commonly detected viruses [13,14]. Mice were monitored during the subsequent 24 h for signs of extreme respiratory distress and culled if symptoms persisted or worsened.

2.9. Locomotor Activity

One day prior to the terminal experiment, locomotor activity was assessed in an open−field arena (60 × 60 × 60 cm) between 08:00 and 13:00 to minimize circadian interference. Mice were allowed to explore freely for 8 min; behavior was recorded and analyzed using EthoVision XT software (v11.5; Noldus Information Technology B.V., Wageningen, The Netherlands) to quantify total distance travelled.

2.10. In Situ Muscle Contractile Function

At study end, mice were anesthetised with ketamine/xylazine (80/16 mg·kg^{-1}). The right hindfoot was secured, the TA was surgically exposed, and the distal tendon was isolated and tied with sutures for attachment to an isometric force transducer. The mouse was transferred to a heated platform (37 °C) mounted to an in situ contractile apparatus (1300A 3−in−1 whole animal system; Aurora Scientific Inc., Aurora, ON, Canada). Two fine electrodes were inserted into the muscle belly (~3–5 mm apart), and the muscle was periodically bathed with warm saline to prevent drying. The TA was stimulated twice at 100 Hz (2 −min rest interval) to settle the preparation. Optimal muscle length (L0) was determined using twitch contractions every 30 s while incrementally adjusting muscle length until maximal twitch force was achieved; L0 was measured as the distance between the distal myotendinous junction and the proximal insertion. A force–frequency protocol was performed at 10, 20, 30, 50, 80, 100, 120, 150, 200, 250, and 300 Hz with 2 −min intervals; forces were recorded using DYNAMIC MUSCLE ANALYSIS software (611A, versions 5.2Aurora Scientific, Aurora, ON, Canada), as previously described [6,29].

2.11. Tissue Collection

At the end of the experimental procedure, mice were terminally anesthetised with sodium pentobarbitone (Lethobarb; 240 mg·kg^{-1}, i.p.), and tissues were harvested. Bronchoalveolar lavage fluid (BALF) was collected via tracheotomy using 400 µL PBS followed by three aliquots of 300 µL ice−cold PBS (≈1 mL total). Hindlimb muscles (TA, quadriceps, and calf components) were dissected and weighed; tissues were snap−frozen in liquid nitrogen for molecular analyses or embedded in optimal cutting temperature (OCT) and frozen in liquid−nitrogen−cooled isopentane for histology. Tibiae were either snap−frozen for PCR analyses or fixed in 10% neutral buffered formalin for 24 h, then

transferred to 70% ethanol and stored at 4 °C until micro−computed tomography (micro−CT) analysis.

2.12. BALF Differential Cell Counts

Total viable BALF cells were quantified by hemocytometer using acridine orange/ethidium bromide staining. Differential cell counts were performed on cytospin preparations (400 rpm, 10 min) stained with rapid red/blue dyes; macrophages, neutrophils, and lymphocytes were identified by standard morphology (≥500 cells per slide), as previously described [6,29].

2.13. Additional Chronic Cigarette Smoke Cohorts

Additional independent cohorts of male BALB/c mice were exposed to cigarette smoke for 2, 4, or 6 months to examine chronic effects on bone−related gene expression and trabecular bone microarchitecture. These cohorts were analyzed independently from the 8−week CS/IAV/ebselen experiment and are presented in Supplementary Figure S1.

2.14. Tibial Micro−CT and Morphometric Analysis

Fixed right tibiae were analyzed using micro−CT (Skyscan 1275, Bruker microCT N.V., Kontich, Belgium) with the following acquisition parameters: 50 kV tube voltage, 100 μA current, frame averaging 2, 0.5 mm aluminum attenuation filter, and 0.5° rotation stepping. Two−dimensional projections were reconstructed using NRecon software (v1.7.3, Bruker microCT N.V., Kontich, Belgium). Bone tissue was segmented using a consistent threshold (40–220 arbitrary units in raw pixel intensity), and morphometry was quantified using Bruker CTAn software (v1.18, Bruker microCT N.V., Kontich, Belgium). Trabecular and cortical volumes of interest were defined relative to the proximal tibial growth plate [30]. The growth−plate reference slice was identified by examining consecutive cross−sections until a continuous low−density cartilage bridge was visible across the section, following disappearance of the last interrupting band of primary spongiosa. Trabecular morphometry was assessed in the proximal tibial metaphysis using manually drawn contours within the cortical shell. Trabecular outcomes included bone volume fraction (BV/TV), trabecular thickness (Tb.Th), trabecular separation (Tb.Sp), and trabecular number (Tb.N). Cortical outcomes included total cross−sectional area (Tt.Ar), cortical area (Ct.Ar), cortical thickness (Ct.Th), and cortical area fraction (Ct.Ar/Tt.Ar).

For the 6−month bone cohort, mice were exposed to whole−body cigarette smoke for 24 weeks using the previously described chronic CS exposure protocol of Chan et al.[29]. At the 6−month endpoint, tibiae were collected for micro−computed tomography assessment of trabecular bone microarchitecture, including BV/TV, Tb.Th, Tb.Sp, and Tb.N.

2.15. Immunofluorescence and Myofiber Analysis

Frozen OCT−embedded TA muscles were equilibrated to −22 °C and sectioned transversely at 4 μm from the widest region of the muscle. Sections were fixed in 4% paraformaldehyde for 10 min, washed in PBS containing Tween 20 (PBST), and blocked for 2 h at room temperature in PBS containing 5% foetal bovine serum, 0.5% Triton X−100, and 0.01% sodium azide. Sections were incubated overnight at 4 °C with fluorophore−conjugated antibodies against laminin (ab11575; Abcam, UK) and slow skeletal muscle myosin heavy chain (clone BA−F8, IgG2b; Developmental Studies Hybridoma Bank, University of Iowa, USA; RRID: AB_10572253), diluted 1:100 in PBST. Sections were then washed, mounted with Fluoromount−G containing DAPI, and imaged at 20× magnification using an Olympus VS120−S5 slide scanner (Olympus Corporation, Tokyo, Japan). Myofiber cross−sectional area (CSA), size distribution, and BA−F8−positive

fiber proportion were quantified using cellSens software (v 1.13, Olympus Corporation, Tokyo, Japan). BA−F8−positive slow myosin heavy−chain fibers were expressed as a percentage of the total myofiber count for each mouse. Quantification was performed within sampling regions of consistent size and anatomical location across samples. BA−F8−positive myofibers and total myofibers were manually counted within each sampled region, and counts from the sampled image fields were combined to calculate the BA−F8−positive fiber proportion for each mouse. Mean myofiber CSA was calculated separately for each mouse and analyzed across all eight experimental groups using three−way ANOVA, as described below, with six mice per group. Pooled fiber−size distributions were presented descriptively. Fiber−level measurements were pooled within each experimental group for descriptive presentation of size distributions. These analyses were performed using established protocols from our laboratory, as previously described [6,26,31].

2.16. Protein Extraction and Western Blotting

Frozen TA muscle was powdered under liquid nitrogen and homogenized in ice−cold RIPA buffer supplemented with β−mercaptoethanol and protease inhibitor cocktail. Homogenates were incubated on ice for 30 min and centrifuged at 14,000× *g* for 10 min at 4 °C, and supernatants were collected for protein quantification using a BCA assay. Protein samples were standardized in Laemmli buffer, denatured at 85 °C for 15 min, separated by SDS−PAGE, and transferred onto PVDF membranes. Membranes were blocked in 5% BSA and incubated overnight at 4 °C with primary antibodies against SERCA2 ATPase (ab150435; Abcam, UK), STIM1 (ab62031; Abcam, UK), and GAPDH (#2118; Cell Signaling Technology, Inc., Danvers, MA, USA), followed by HRP−conjugated secondary antibodies. Bands were visualized using chemiluminescence and imaged using a ChemiDoc system (Bio−Rad Laboratories, Inc., Hercules, CA, USA−), and densitometry was performed using Image Lab software (version 6.1.0, build 7; Bio-Rad Laboratories, Inc., Hercules, CA, USA). For membranes analyzed sequentially for STIM1 and SERCA2, STIM1 was detected first and quantified from the initial acquisition at approximately 85–86 kDa. The same membrane was subsequently probed for SERCA2, which was quantified from the subsequent acquisition at approximately 115 kDa. SERCA2 and STIM1 band intensities were normalized to GAPDH and expressed as fold−change relative to the relevant control group.

2.17. OxyBlot Analysis

Protein carbonylation was assessed using the OxyBlot Protein Oxidation Detection Kit according to the manufacturer's instructions. Briefly, 10 μg of TA muscle protein was derivatized for immunoblot detection of carbonyl groups, separated by SDS−PAGE and transferred onto PVDF membranes. Membranes were blocked, incubated overnight with the kit primary antibody, followed by the supplied secondary antibody, and developed using chemiluminescent substrate. OxyBlot signal was quantified by densitometry using Image Lab software (version 6.1.0, build 7; Bio-Rad Laboratories, Inc., Hercules, CA, USA). Equal amounts of protein (10 μg per lane) were loaded, and total lane carbonylation signal was quantified by densitometry without additional housekeeping−protein normalization, as previously described [6,26].

2.18. Quantitative Real−Time PCR

Frozen tissue was powdered under liquid nitrogen and homogenized in Buffer RLT using a TissueLyser LT (QIAGEN, Germantown, MD, USA). Total RNA was extracted using the RNeasy Mini Kit (QIAGEN, Germantown, MD, USA), quantified using a NanoDrop spectrophotometer, and 1 μg RNA was reverse transcribed using the

High−Capacity RNA−to−cDNA Kit (Thermo Fisher Scientific, Waltham, MA, USA). Quantitative PCR was performed using pre−designed mouse TaqMan Gene Expression Assays (Applied Biosystems/Thermo Fisher Scientific, Waltham, MA, USA) for *Ibsp* (Mm00492555_m1; RefSeq NM_008318.3), *Bglap* (Mm03413826_mH; RefSeq NM_001037939.2 and NM_007541.3), and *Spp1* (Mm00436767_m1; RefSeq NM_001204201.1, NM_001204202.1, NM_001204203.1, NM_001204233.1, and NM_009263.3). *Ppil3* (Mm00510343_m1; mouse RefSeq transcripts NM_001285826.1, NM_001285827.1, NM_027351.3, and NM_027374.3) was used as the endogenous reference gene. Reactions were performed in technical triplicate on a QuantStudio 7 instrument. The mean Ct value of the technical replicates was calculated for each biological sample, and ΔCt was determined as Ct(target gene)—Ct(*Ppil3*). Relative gene expression was calculated using the comparative $2^{-\Delta\Delta Ct}$ method relative to the corresponding time−matched Sham control.

2.19. Statistical Analysis

Data are presented as mean + SEM, with individual mice as the experimental units unless otherwise stated. Unless otherwise specified, CS and IAV effects were assessed within vehicle− or ebselen−treated groups using two−way ANOVA followed by Tukey's multiple−comparisons test. For mean myofiber CSA and BA−F8−positive fiber proportion, one mouse−level value was used for each biological replicate, with six mice per experimental group. Pooled fiber−size distributions were presented descriptively. Treatment−related effects were evaluated using the combined factorial models described below.

TA force–frequency responses were analyzed jointly across all eight experimental groups using factorial repeated−measures ANOVA, with CS, IAV, and ebselen as between−animal factors and stimulation frequency as the within−animal factor. All main effects and interactions were included, and Greenhouse–Geisser correction was applied to frequency−related tests ($\varepsilon = 0.27517$). Mean myofiber CSA, specific force, distance travelled, BA−F8−positive fiber proportion, protein carbonylation, SERCA2/GAPDH, and STIM1/GAPDH were analyzed separately using three−way ANOVA incorporating CS, IAV, and ebselen, including all main effects and interactions. These models used Type III sums of squares with sum−to−zero contrasts. Distance travelled was natural−log transformed before analysis. For BA−F8−positive fiber proportion, vehicle−versus−ebselen comparisons within Sham mice under PBS and IAV conditions were estimated from the combined model, with Holm adjustment across these two comparisons.

Residual normality and homogeneity of variance were assessed using Shapiro–Wilk and median−centered Levene tests, respectively. Sensitivity analyses using an HC3 heteroscedasticity−robust covariance estimator were performed for trabecular separation, protein carbonylation, and STIM1. For quantitative PCR, statistical testing was performed on ΔCt values. Sham and CS groups were compared separately at each exposure duration using two−tailed unpaired Student's t−tests. Relative expression was displayed as $2^{-\Delta\Delta Ct}$ fold change.

Factorial effect estimates and pointwise 95% confidence intervals for selected endpoints are provided in Supplementary Table S2. These confidence intervals were not adjusted for multiple testing; multiplicity adjustment for within−treatment pairwise comparisons was performed using Tukey's procedure. Analyses were performed using GraphPad Prism 9, except for the combined factorial analyses and HC3 sensitivity analyses, which used Python (https://www.python.org/, accessed on 16 November 2026) with NumPy (https://numpy.org/, accessed on 16 November 2026), SciPy (https://scipy.org/, accessed on 16 November 2026), and statsmodels

(https://www.statsmodels.org/, accessed on 16 November 2026). Statistical significance was set at $p \leq 0.05$.

3. Results

3.1. CS Exposure and Acute IAV Infection Establish a Robust Inflammatory Airway Phenotype

To model acute viral exacerbation of COPD, mice were exposed to CS for 8 weeks before intranasal IAV challenge, with parallel ebselen treatment used to examine treatment−associated differences in skeletal muscle outcomes (Figure 1A,B). We first confirmed that the model induced the expected pulmonary inflammatory response by BALF differential cell count. CS exposure alone increased total BALF cell numbers by ~14−fold relative to sham/PBS controls, whereas total BALF cell counts in Sham Veh IAV mice were approximately 11−fold higher than in Sham Veh PBS controls (Tukey−adjusted $p < 0.0001$; Figure 2A). The combined CS + IAV group showed the greatest inflammatory burden, with total BALF cells increasing by ~35−fold, indicating that smoke exposure and viral infection each independently drive airway inflammation but together produce the most pronounced response. A similar pattern was seen across BALF leukocyte populations, including macrophages, neutrophils, and lymphocytes (Figure 2B–D), confirming acute exacerbation.

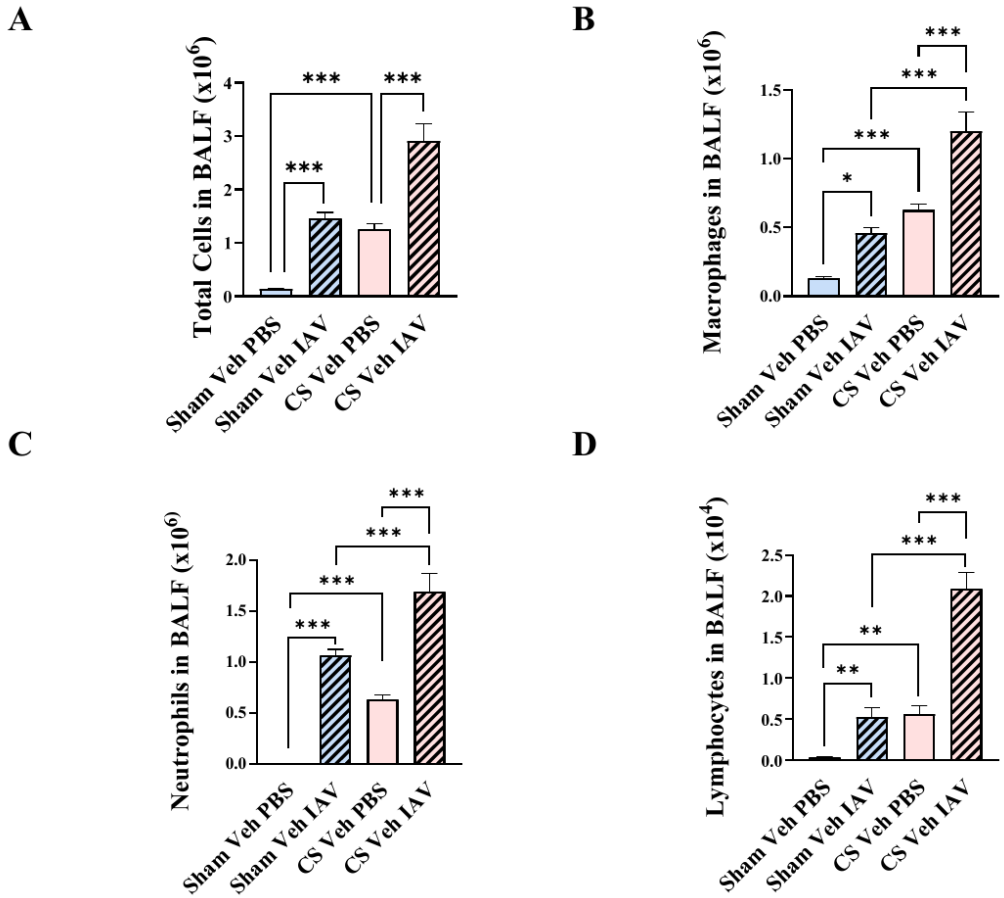

Figure 2. Cigarette smoke exposure and acute influenza A virus infection increase airway inflammatory cell burden. Bronchoalveolar lavage fluid (BALF) was collected at day 3 post−infection from vehicle−treated mice exposed to room air (Sham) or CS, followed by PBS or influenza A virus (IAV) challenge. Quantification of (**A**) total BALF cells, (**B**) macrophages, (**C**) neutrophils, and (**D**) lymphocytes showed increased airway inflammatory cellularity following CS exposure and/or IAV infection, with the combined CS Veh IAV group showing the greatest inflammatory burden. Data are presented as mean + SEM ($n = 8$ mice/group). * $p < 0.05$, ** $p < 0.01$, *** $p < 0.001$.

3.2. CS Exposure and Acute IAV Infection Differentially Alter Trabecular Bone Microarchitecture

CS exposure markedly altered trabecular bone architecture, reducing BV/TV by 57% and increasing trabecular separation relative to Sham PBS controls (Figure 3A–D). In Sham mice, acute IAV infection was associated with a 38% reduction in BV/TV. Two−way ANOVA identified a significant CS × IAV interaction for BV/TV ($F(1, 28) = 24.70$, $p < 0.0001$), indicating that the effect of IAV on these trabecular outcomes depended on prior CS exposure. A significant CS × IAV interaction was also detected for trabecular separation ($F(1, 28) = 9.30$, $p = 0.005$), indicating that the IAV−associated difference depended on CS exposure. Mean separation was higher following IAV challenge in Sham mice but lower in CS−exposed mice. No significant interaction was detected for trabecular thickness ($F(1, 28) = 4.19$, $p = 0.0502$) or trabecular number ($F(1, 28) = 1.89$, $p = 0.180$). For cortical outcomes, CS exposure had a significant main effect on cortical area and cortical thickness; the CS × IAV interaction was not significant for cortical area ($F(1, 28) = 3.90$, $p = 0.0583$) but was significant for cortical thickness ($F(1, 28) = 5.11$, $p = 0.0318$) (Figure 3F–G).

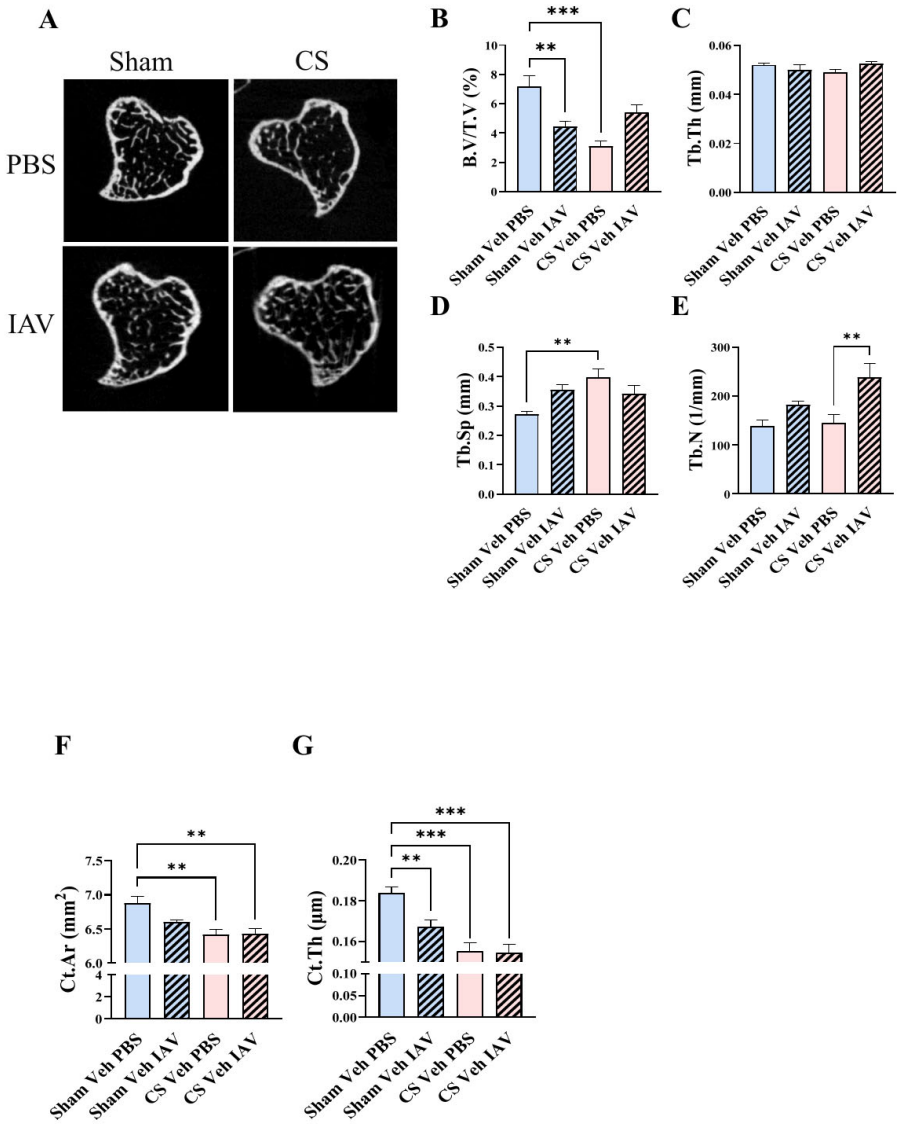

Figure 3. Cigarette smoke exposure and acute influenza A virus infection differentially alter tibial bone microarchitecture. Tibial micro−computed tomography was performed in vehicle−treated mice exposed to room air (Sham) or CS, followed by PBS or IAV challenge. (**A**) Representative micro−CT images of the proximal tibial trabecular region. Quantification of trabecular parameters

included (**B**) bone volume fraction (BV/TV), (**C**) trabecular thickness (Tb.Th), (**D**) trabecular separation (Tb.Sp), and (E) trabecular number (Tb.N). (**F**) Cortical area (Ct.Ar) and (**G**) cortical thickness (Ct.Th). Two−way ANOVA identified significant CS × IAV interactions for BV/TV, Tb.Sp, and Ct.Th, indicating context−dependent effects of IAV according to prior CS exposure. No significant interaction was detected for Tb.Th, Tb.N, or Ct.Ar. Data are presented as mean + SEM (n = 8 mice/group). , ** $p < 0.01$, *** $p < 0.001$.

3.3. Chronic CS Exposure Suppresses Osteogenic Matrix Gene Expression and Impairs Trabecular Bone Microarchitecture

To provide additional context regarding the effects of chronic cigarette smoke exposure on skeletal homeostasis, independent cohorts exposed to cigarette smoke for 2, 4 or 6 months were analyzed. Cigarette smoke exposure was associated with reduced expression of the osteogenic matrix−associated genes *Ibsp*, *Spp1,* and *Bglap*, with the most consistent suppression observed at 4 months (Figure S1A). In addition, chronic cigarette smoke exposure reduced trabecular bone volume fraction and altered trabecular microarchitecture following 6 months of exposure (Figure S1B).

3.4. CS Exposure, but Not Acute IAV Infection, Selectively Reduces Tibialis Anterior, Gastrocnemius, and Quadriceps Muscle Mass

We next examined whether the skeletal phenotype was accompanied by changes in hindlimb muscle mass. CS exposure selectively reduced the mass of the TA, gastrocnemius, and quadriceps muscles. TA muscle weight was significantly lower in CS−exposed mice than in their corresponding Sham controls under both PBS− and IAV−treated conditions (Figure 4A). Gastrocnemius and quadriceps muscle weights were also significantly reduced in CS−exposed mice relative to their corresponding sham controls under both PBS− and IAV−treated conditions (Figure 4D,E). In contrast, soleus and plantaris muscle weights were not detectably altered across groups (Figure 4B,C). Acute IAV infection alone had no detectable effect on muscle mass, nor did it clearly exacerbate the reductions associated with CS exposure.

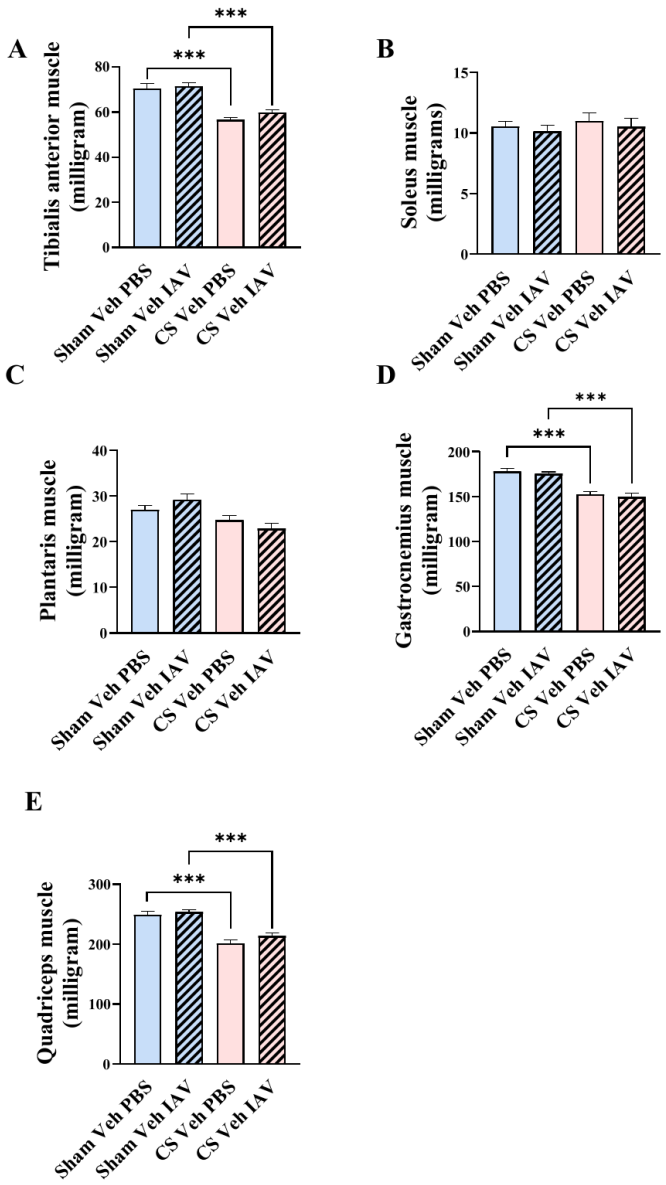

Figure 4. Cigarette smoke exposure selectively reduces hindlimb muscle mass in vehicle−treated mice. Hindlimb muscles were dissected and weighed at day 3 post−infection from vehicle−treated mice exposed to room air (Sham) or CS, followed by PBS or IAV challenge. Muscle weights were quantified for (**A**) tibialis anterior, (**B**) soleus, (**C**) plantaris, (**D**) gastrocnemius, and (**E**) quadriceps muscles. Dissected muscle weights are reported as absolute wet weights and were not normalized to body weight. CS exposure reduced tibialis anterior, gastrocnemius, and quadriceps muscle weights, whereas soleus and plantaris muscle weights were not detectably altered. Acute IAV infection alone did not clearly reduce hindlimb muscle mass or further exacerbate CS−associated muscle mass loss. Data are presented as mean+ SEM (n = 6 mice/group). *** $p < 0.001$.

In support of a broader systemic wasting phenotype, CS exposure also reduced body weight trajectory, whole−body fat and lean mass, and epididymal and retroperitoneal fat depots, with little evidence that IAV infection alone drove these changes (Figure S2A–E). Muscle weights in ebselen−treated mice are presented separately (Figure S3). These within−treatment summaries do not establish whether the CS−associated muscle−weight differences varied according to ebselen treatment; a direct combined analysis would be required to test that question.

3.5. CS Exposure and Acute IAV Infection Alter TA Contractile Function

In vehicle−treated mice, mean TA force responses were lower following CS exposure and/or IAV challenge, with the lowest responses observed in CS Veh IAV mice at higher stimulation frequencies (Figure 5A). Combined analysis identified a CS × ebselen interaction ($F(1, 40) = 6.57$, $p = 0.014$), together with CS × ebselen × frequency ($F(2.75, 110.07) = 9.00$, $p < 0.001$) and IAV × ebselen × frequency interactions ($F(2.75, 110.07) = 3.91$, $p = 0.013$; Figure 5A,B). Neither the CS × IAV × ebselen interaction nor its interaction with frequency was significant ($p = 0.841$ and 0.354, respectively). Specific force showed CS × ebselen ($F(1, 40) = 8.21$, $p = 0.007$), IAV × ebselen ($F(1, 40) = 5.05$, $p = 0.030$), and CS × IAV interactions ($F(1, 40) = 10.59$, $p = 0.002$), but no CS × IAV × ebselen interaction ($F(1, 40) = 0.57$, $p = 0.454$; Figure 5C,D). Together, these findings indicate treatment−dependent differences in contractile responses, but do not establish that ebselen specifically modified the CS × IAV interaction. For spontaneous locomotor activity, analysis of log−transformed distance travelled identified a CS × IAV interaction ($F(1, 40) = 4.88$, $p = 0.033$; Figure 5E,F). No main effect of ebselen or interaction involving ebselen was detected (all $p \geq 0.333$).

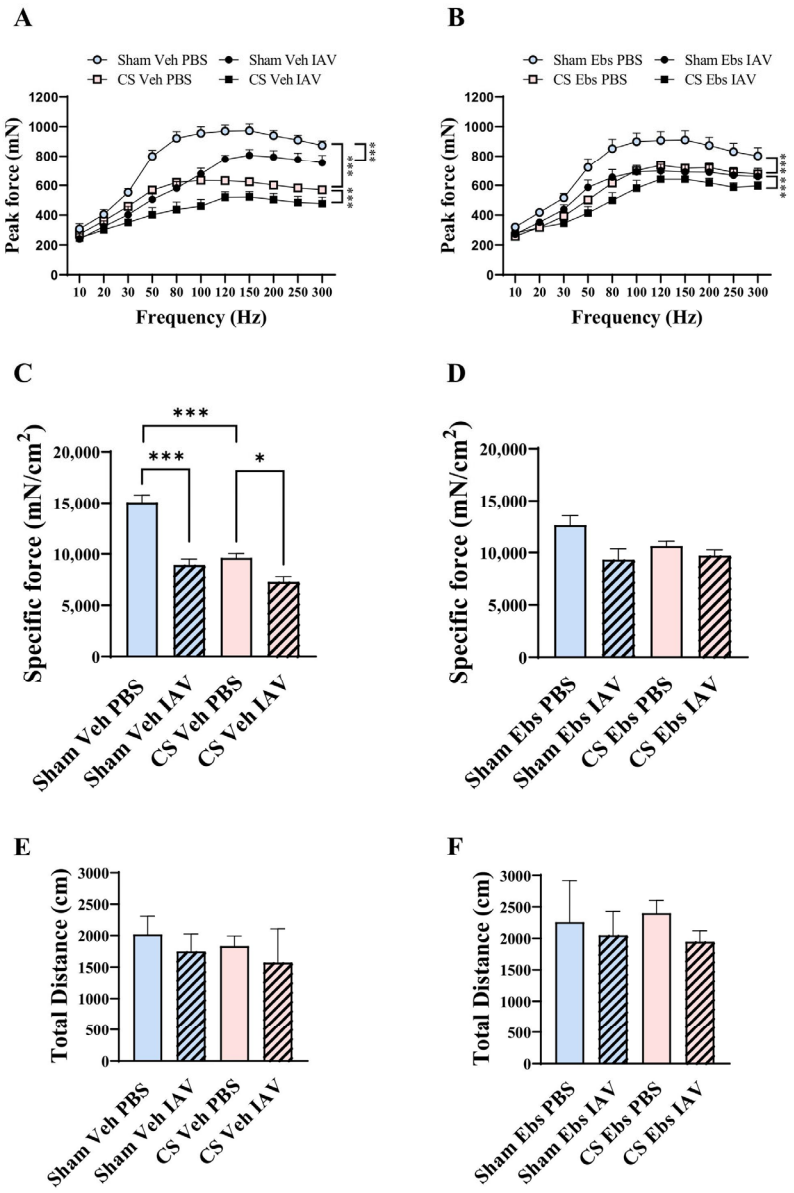

Figure 5. Tibialis anterior contractile function and spontaneous locomotor activity following cigarette smoke exposure, IAV challenge, and ebselen treatment. TA contractile function was

assessed at day 3 post−infection, and locomotor activity was assessed one day before the terminal experiment. Force–frequency responses are shown for (**A**) vehicle− and (**B**) ebselen−treated mice. Specific force is shown for (**C**) vehicle− and (**D**) ebselen−treated mice. Total distance travelled is shown for (**E**) vehicle− and (**F**) ebselen−treated mice. Panels A–B were analyzed jointly using factorial repeated−measures ANOVA with Greenhouse–Geisser correction. Specific force and natural−log−transformed distance travelled were analyzed separately using three−way ANOVA incorporating CS, IAV, and ebselen, including all interactions. Data are presented as mean + SEM (n = 6 mice/group). * $p < 0.05$, *** $p < 0.001$.

3.6. Myofiber Measurements Describe Differences in Fibre Size Across Experimental Groups

We next examined TA myofiber morphology (Figure 6A–D). Three−way ANOVA of mouse−level mean CSA identified a significant CS × ebselen interaction ($F(1, 40) = 14.08$, $p = 0.0006$; Figure 6B), indicating that the CS−associated difference varied according to ebselen treatment. Mean CSA was lower in CS−exposed vehicle−treated groups, whereas the corresponding difference was smaller in ebselen−treated groups. The CS × IAV × ebselen interaction was not significant ($F(1, 40) = 2.97$, $p = 0.0928$). Pooled fiber−size distributions are presented descriptively for vehicle− and ebselen−treated groups (Figure 6C,D, respectively).

3.7. CS−Associated Differences in BA−F8−Positive Fiber Proportion Depend on Ebselen Treatment

Three−way ANOVA identified a significant CS × ebselen interaction for BA−F8−positive fiber proportion ($F(1, 40) = 11.15$, $p = 0.0018$; Figure 6F), indicating that the CS−associated difference varied according to ebselen treatment. Descriptively, the lower proportion observed in CS−exposed vehicle−treated mice was less pronounced in ebselen−treated mice. Neither the IAV × ebselen interaction nor the CS × IAV × ebselen interaction was significant ($p = 0.8916$ and 0.8716, respectively). Model−based comparisons did not detect differences between vehicle− and ebselen−treated Sham mice under either PBS or IAV conditions (Holm−adjusted $p = 1.000$ for both comparisons).

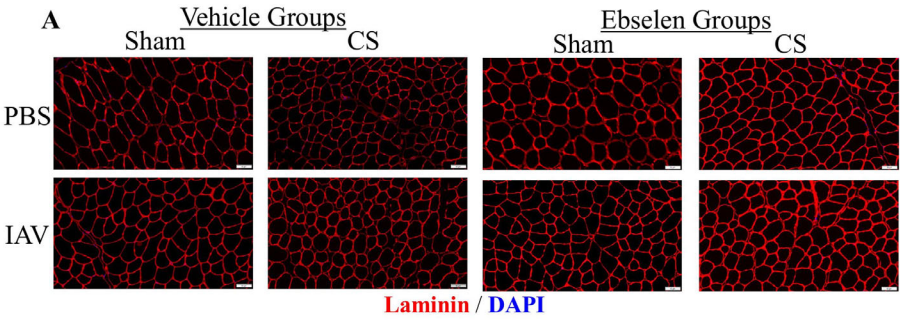

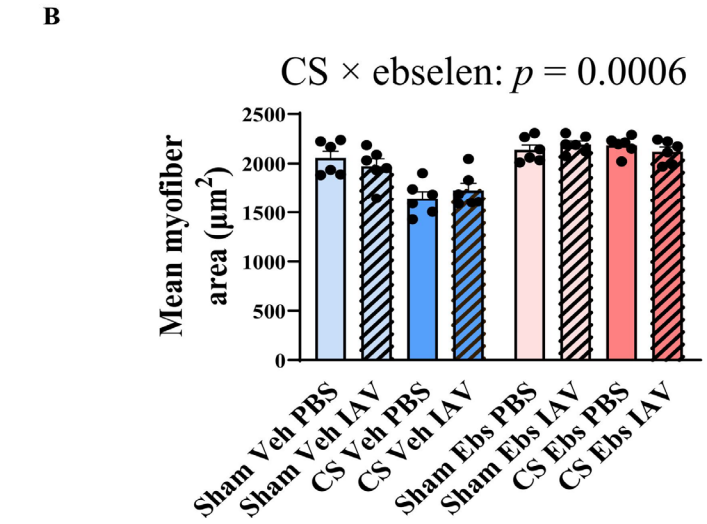

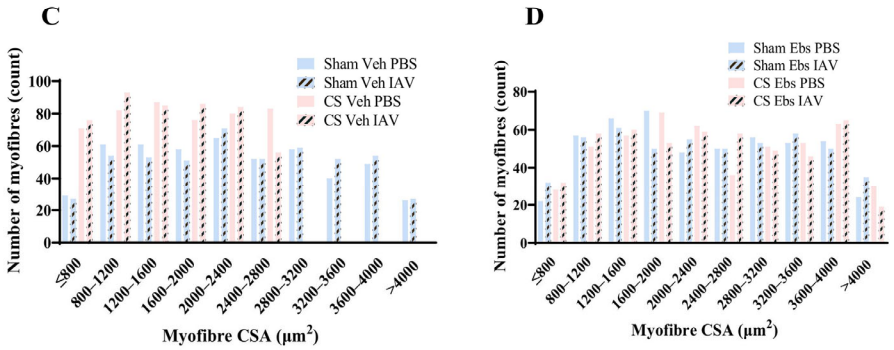

https://doi.org/10.3390/antiox15121542

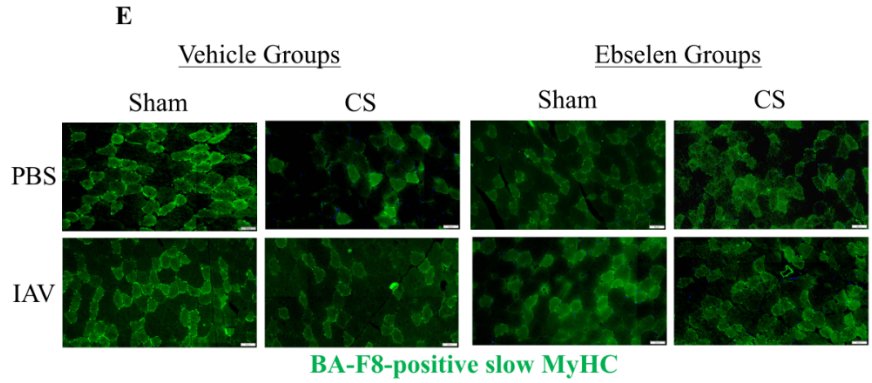

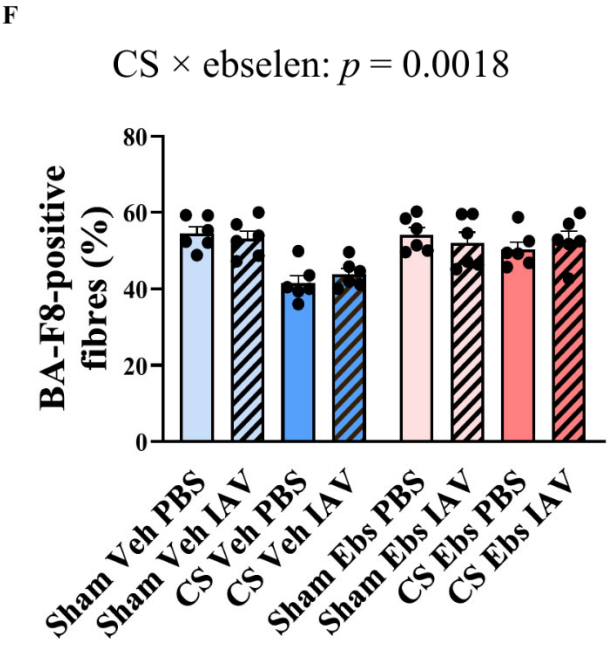

Figure 6. Tibialis anterior myofiber morphology and BA−F8−positive fiber proportion following cigarette smoke exposure, IAV challenge, and ebselen treatment. TA muscle sections were assessed at day 3 post−infection. (**A**) Representative laminin−stained cross−sections from all eight experimental groups. Laminin is shown in red and DAPI−stained nuclei in blue. (**B**) Mean myofiber cross−sectional area (CSA). Each point represents the mean CSA for one mouse, calculated from the fibers measured across that mouse's sampled image fields. Bars show the group mean + SEM (n = 6 mice per group). Data were analyzed using three−way ANOVA incorporating CS, IAV, and ebselen, including all main effects and interactions. A significant CS × ebselen interaction was detected ($F(1, 40) = 14.08$, $p = 0.0006$), whereas the CS × IAV × ebselen interaction was not significant ($F(1, 40) = 2.97$, $p = 0.0928$). The annotation above panels B and F denote the CS × ebselen interactions for mean CSA (p = 0.0006) and BA−F8−positive fiber proportion (p = 0.0018), respectively, rather than pairwise comparisons. (**C**,**D**) Pooled fiber−size distributions for vehicle− and ebselen−treated groups, respectively, presented descriptively. (**E**) Representative BA−F8 immunofluorescence images from all eight experimental groups, with staining shown in green. (**F**) BA−F8−positive fiber proportion, calculated as the number of BA−F8−positive myofibers divided by the total myofiber count for each mouse and expressed as a percentage. Each point represents one mouse, and bars show the group mean + SEM (n = 6 mice per group). Data were analyzed using three−way ANOVA incorporating CS, IAV, and ebselen, including all main effects and interactions.

3.8. Protein Carbonylation and Calcium–Handling Protein Expression Show Distinct Treatment–Related Patterns

We assessed protein carbonylation and the abundance of SERCA2 and STIM1 in TA muscle. Combined three–way ANOVA of protein carbonylation did not detect significant main effects or interactions (Figure 7A–C). The absence of significant treatment–related interactions was unchanged in the HC3 sensitivity analysis. The CS × ebselen ($F(1, 40) = 2.69$, $p = 0.109$), IAV × ebselen ($F(1, 40) = 2.66$, $p = 0.111$), and CS × IAV × ebselen interactions ($F(1, 40) = 1.52$, $p = 0.225$) were not significant. In contrast, CS × IAV × ebselen interactions were detected for SERCA2/GAPDH ($F(1, 40) = 11.82$, $p = 0.001$) and STIM1/GAPDH ($F(1, 40) = 32.24$, $p < 0.001$; Figure 7D–F), indicating that the CS × IAV interaction differed according to ebselen treatment. Both proteins had their highest mean abundance in CS Veh IAV mice, whereas this pattern was not apparent in ebselen–treated mice. The STIM1 three–way interaction remained significant in a heteroscedasticity–robust sensitivity analysis ($F(1, 40) = 26.86$, $p < 0.001$).

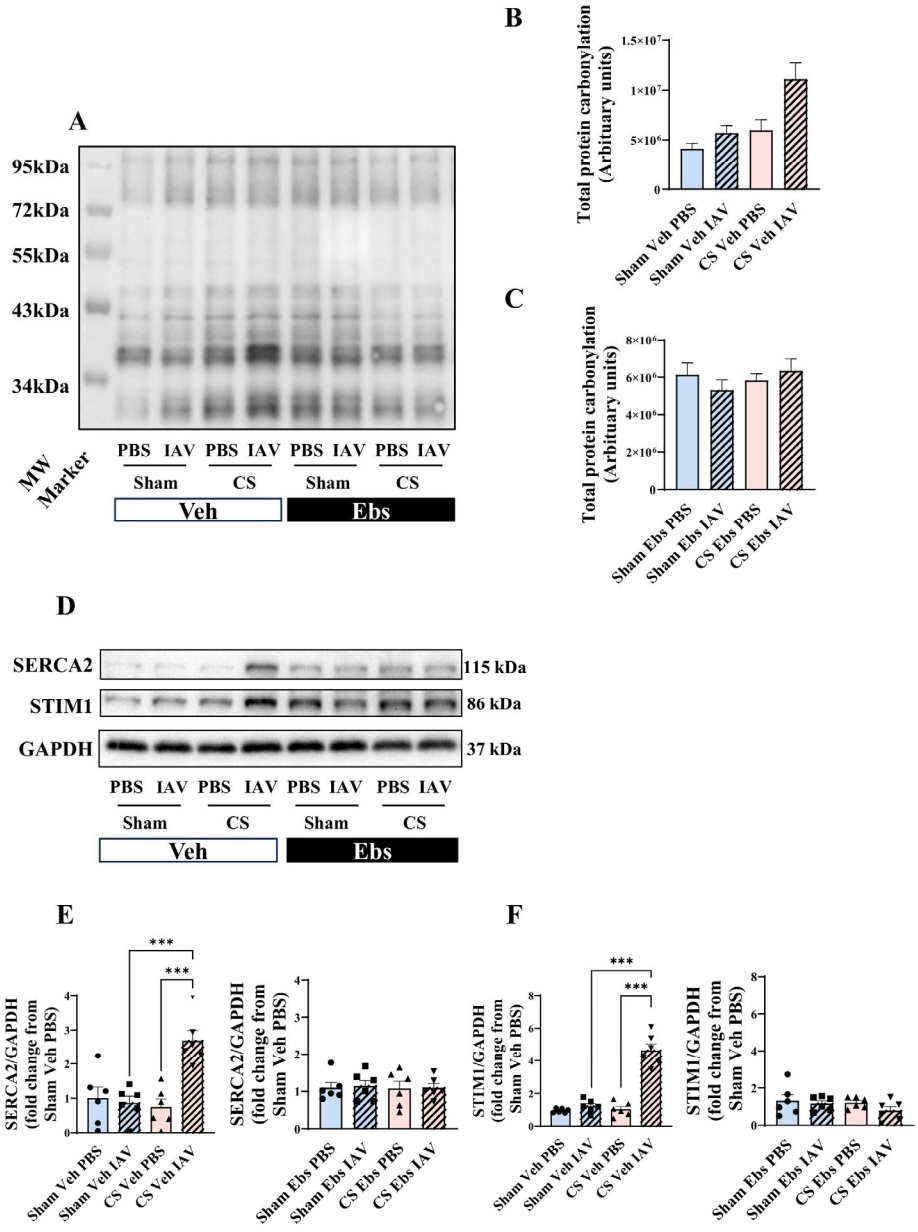

Figure 7. Protein carbonylation and calcium–handling protein expression in tibialis anterior muscle. Oxidative protein modification and calcium–handling protein expression were assessed in tibialis

anterior muscle homogenates from vehicle− and ebselen−treated mice exposed to room air (Sham) or CS, followed by PBS or IAV challenge. (**A**) Representative OxyBlot showing protein carbonylation across multiple molecular weights, with corresponding densitometric quantification of the total lane signal. Equal amounts of protein (10 µg per lane) were loaded, and no additional housekeeping−protein normalization was applied. Molecular weights are indicated in kDa. (**B**,**C**) Total lane carbonylation signal in vehicle− and ebselen−treated mice, respectively. Panels B–C were analyzed jointly using three−way ANOVA; no significant main effects or interactions were detected. (**D**) Representative Western blot images for SERCA2 (115 kDa), STIM1 (86 kDa), and GAPDH (37 kDa). (**E**) SERCA2/GAPDH and (**F**) STIM1/GAPDH abundance. Individual points represent separate mice. Each endpoint was analyzed across all eight groups using three−way ANOVA, which identified a CS × IAV × ebselen interaction. Data are presented as mean + SEM (n = 6 mice/group). *** $p < 0.001$. SERCA2, sarco/endoplasmic reticulum Ca^{2+}−ATPase 2; STIM1, stromal interaction molecule 1.

4. Discussion

This study demonstrates that CS exposure and acute IAV infection exert distinct but intersecting effects on the musculoskeletal system in a preclinical model of AECOPD. Three principal findings emerge from this work. First, acute IAV infection was associated with a rapid alteration in trabecular bone microarchitecture, with reductions in BV/TV evident within 3 days of infection. Second, acute viral challenge was associated with impaired skeletal muscle force generation, with the lowest mean responses observed in the combined CS/IAV vehicle group despite limited evidence of additional muscle wasting. These findings support a dissociation between muscle mass and contractile performance. Third, treatment−related interactions were detected for contractile outcomes, mean myofiber CSA, and BA−F8−positive fiber proportion, whereas the combined protein−carbonylation analysis did not detect significant main effects or interactions. The combined force–frequency analysis identified a CS × ebselen interaction, indicating that treatment−associated force differences varied with smoke exposure. However, neither the CS × IAV × ebselen interaction nor its interaction with frequency was statistically significant. These findings therefore do not establish that ebselen specifically modifies the interaction between CS exposure and acute IAV infection.

A notable finding was the lower trabecular BV/TV in IAV−challenged Sham mice at day 3 post−infection, with a significant CS × IAV interaction indicating that the IAV−associated difference depended on prior CS exposure. COPD−associated bone loss is commonly attributed to chronic factors such as smoking, systemic inflammation, physical inactivity, altered body composition, and disrupted muscle–bone crosstalk [10,32]. The present findings identify an acute infection−associated difference in trabecular microarchitecture, although the absence of baseline longitudinal measurements prevents determination of the within−animal change over this interval. However, because dynamic histomorphometry, osteoclast activity, and bone turnover markers were not assessed at this acute endpoint, these data should be interpreted as evidence of altered bone microarchitecture rather than definitive proof of accelerated bone resorption or remodeling. The acute 3−day endpoint also does not establish whether these microarchitectural changes are transient, reversible, or persistent. This is consistent with osteoimmunological principles, whereby infection and immune activation can alter the balance between bone formation and resorption through inflammatory mediators and immune–bone interactions [18]. In parallel, CS exposure suppressed osteogenic matrix−related genes, including *Ibsp*, *Spp1*, and *Bglap*, and produced structural trabecular deterioration [33–35], consistent with altered osteogenic gene expression and bone microarchitecture, without directly establishing changes in bone formation rate. These gene−expression measurements were obtained from independent chronic CS cohorts and

therefore provide complementary evidence of chronic CS–associated osteogenic alterations rather than a direct mechanistic explanation for the acute IAV–associated reduction in BV/TV. The lack of additive deterioration in the CS + IAV group may indicate that a single viral challenge was insufficient to worsen an already CS–exposure–injured bone compartment [19,20] or that different mechanisms converge on a similar trabecular endpoint.

The differential effects of CS exposure and IAV infection on hindlimb bone and muscle suggest that these musculoskeletal compartments respond differently to chronic and acute respiratory insults [4]. Both CS exposure and IAV infection impaired trabecular bone structure, whereas measurable muscle mass loss and fiber–type remodeling were primarily driven by CS exposure. This supports the concept that bone may be acutely sensitive to systemic inflammatory or osteoimmune perturbation during viral infection [18,36–38], while muscle wasting may require a more sustained catabolic exposure [5,7,39,40]. This interpretation is consistent with our previous work showing that IAV–driven airway inflammation can worsen TA force–generating capacity without necessarily causing additional limb muscle mass loss in smoke–exposed mice [6]. Thus, muscle mass and contractile performance appear partially dissociated: CS exposure was associated with lower selected muscle weights and altered myofiber morphology, whereas the combined CS/IAV vehicle group showed the lowest mean force responses without clear additional muscle mass loss. Altered SERCA2/STIM1 abundance accompanied this phenotype, but the combined protein–carbonylation analysis did not detect significant main effects or interactions.

The skeletal muscle findings demonstrate differences in force generation, BA–F8–positive fiber proportion, and calcium–handling protein abundance across exposure and treatment conditions. Although oxidative stress has been implicated in COPD–associated skeletal muscle dysfunction [17,26,31], the present protein–carbonylation analysis did not detect significant main effects or interactions. The ebselen–associated differences therefore cannot be attributed to a demonstrated change in oxidative protein damage or redox signaling. Given the antioxidant and anti–inflammatory properties of ebselen, the mechanisms underlying these treatment–associated differences require direct investigation.

The TA muscle may be particularly susceptible to oxidative and metabolic stress because of its fiber composition. The TA is a predominantly fast–twitch, glycolytic muscle, whereas more oxidative muscles generally possess greater mitochondrial content and antioxidant reserve [17,41]. Oxidative muscles have been reported to maintain more robust mitochondrial homeostasis than glycolytic muscles, while glycolytic muscles such as TA appear more susceptible to mitochondrial functional decline under stress conditions [41,42]. This is relevant here because the TA showed CS–exposure–induced mass loss, impaired force generation, reduced myofiber CSA, a lower BA–F8–positive fiber proportion, and altered calcium–handling protein abundance. One interpretation is that the fast–fiber–predominant TA has lower intrinsic oxidative reserve and may therefore be less redox robust during combined smoke and viral stress. The CS–induced loss of BA–F8–positive fiber proportion may further reduce metabolic flexibility [43], making the muscle more susceptible to acute viral exacerbation [10,17]. However, this remains a hypothesis and should be tested directly by assessing fiber–type–specific oxidative damage, antioxidant capacity, and mitochondrial respiration.

Combined analyses identified CS × IAV × ebselen interactions for SERCA2 and STIM1 abundance. These findings indicate that the CS × IAV–associated expression patterns differed according to treatment, but do not establish altered calcium transport or a causal redox mechanism. SERCA proteins regulate sarcoplasmic reticulum calcium reuptake, while STIM1 contributes to store–operated calcium entry and calcium homeostasis [44–

46]. It is also possible that the increased SERCA2 and STIM1 abundance reflects altered fiber−type biology, a calcium−handling stress response, or a compensatory remodeling response rather than direct evidence of calcium dysfunction. These possibilities require direct experimental evaluation. The functional significance of these expression changes requires direct assessment of calcium handling and excitation–contraction coupling; their relationship to oxidative stress was not established in the present study [43,47,48].

Clinically, these findings reinforce the need to consider COPD exacerbations as systemic events rather than isolated respiratory episodes [10,17]. The association between acute IAV infection and lower trabecular BV/TV raises the possibility that viral exacerbations contribute to skeletal fragility, particularly in patients with pre−existing osteopenia, osteoporosis, or smoking−related bone loss [10,19,21]. Similarly, the dissociation between muscle mass and muscle function suggests that exacerbation−related weakness may occur even without overt additional wasting, which has been observed clinically [49,50]. This has implications for clinical assessment, as body weight or lean mass alone may underestimate muscle dysfunction during or after exacerbation [5,8,51]. The ebselen−associated differences warrant further preclinical investigation, including studies designed to identify the underlying mechanisms and determine whether treatment initiated during acute exacerbation modifies skeletal muscle outcomes.

Several limitations should be acknowledged. First, the study used a single acute IAV challenge after 8 weeks of CS exposure, whereas patients with COPD commonly experience recurrent exacerbations over time [52–54]. The single 3−day post−infection endpoint also precludes conclusions about whether the observed IAV−associated changes in bone microarchitecture are transient, reversible, or persistent. Although body weight was monitored throughout the experiment, food intake and hydration status were not independently quantified, and their potential contributions to the acute bone phenotype cannot be excluded. Bone histomorphometry, osteoclast activity, osteoblast function, and circulating bone−turnover markers were not assessed, limiting mechanistic interpretation of the trabecular findings. In addition, tibial−length measurements were unavailable, preventing assessment of whether differences in longitudinal growth or overall skeletal size contributed to the observed microarchitectural changes. The original micro−CT datasets were unavailable for additional three−dimensional reconstruction or reanalysis, and the exact numerical VOI offsets, longitudinal extent, and voxel size could not be recovered from the available records. These limitations restrict independent verification and full reproducibility of the micro−CT findings.

Lung viral load and viral replication were not measured. Consequently, the study cannot distinguish differences in viral burden from differences in host inflammatory responsiveness, and a potential effect of ebselen on infection severity cannot be excluded. Furthermore, ebselen was administered throughout the CS exposure period before IAV challenge. The design therefore cannot separate effects arising during chronic CS exposure from those specifically associated with the acute viral challenge, nor does it establish efficacy when treatment is initiated during an exacerbation. Only male BALB/c mice were studied, leaving sex−specific responses and generalizability to female mice or other strains unresolved.

The mechanistic interpretation of the muscle findings is also limited by the absence of direct measurements of mitochondrial respiration, antioxidant enzyme activity, ROS−generating pathways and fiber−type−specific oxidative damage. Because CS exposure reduced body weight, the absolute muscle−weight differences cannot distinguish muscle−specific wasting from changes associated with overall body size. Finally, altered SERCA2 and STIM1 abundance does not establish functional calcium−handling abnormalities. Direct measurements of calcium flux and excitation–

contraction coupling are required to determine the functional significance of these protein−expression changes.

In conclusion, this study shows that CS exposure and acute IAV infection differentially affect bone and skeletal muscle during experimental viral exacerbation of COPD. CS exposure was associated with systemic wasting, smaller myofibers, a lower BA−F8−positive fiber proportion and muscle weakness, whereas acute IAV infection reduced trabecular BV/TV in Sham mice and was associated with impaired TA force generation. Ebselen−related interactions were detected for contractile outcomes, mean myofiber CSA, and BA−F8−positive fiber proportion, but not for protein carbonylation. These findings identify distinct skeletal muscle responses associated with ebselen treatment without establishing a redox mechanism while also identifying trabecular bone as an acutely responsive extrapulmonary compartment following respiratory viral infection.

Supplementary Materials: The following supporting information can be downloaded at: https://www.mdpi.com/article/10.3390/antiox15121542/s1, Figure S1: Cigarette smoke exposure suppresses bone matrix gene expression and impairs trabecular bone microarchitecture during chronic exposure; Figure S2: Cigarette smoke exposure reduces body weight, body composition and adipose tissue mass following influenza A virus challenge; Figure S3: Hindlimb muscle weights in ebselen-treated mice following cigarette smoke exposure and influenza A virus challenge. Table S1. Initial group allocation and number of animals contributing to each endpoint measurement; Table S2. Factorial effect estimates and 95% confidence intervals.

Author Contributions: Concept and Design: R.V. and S.M.H.C.; Acquisition of Data: K.M., S.M.H.C., and S.N.D.L.; Data Analysis and Interpretation: K.M., S.M.H.C., R.V., S.N.D.L., H.W., S.S., and S.B.; Drafting, Editing, and/or Critical Revision of the Manuscript for Intellectual Content: All Authors; R.V. Also Provided all Resources for the Work and is the Senior Investigator, Ensuring Accuracy and Integrity. All authors have read and agreed to the published version of the manuscript.

Funding: This Work was Supported by National Health and Medical Research Council of Australia Project Grants APP1084627 and APP1138915. the Funding Body Had no Role in Study Design, Data Collection, Analysis, Interpretation, Manuscript Preparation or the Decision to Publish.

Institutional Review Board Statement: The animal study protocol was approved by the RMIT University Animal Ethics Committee under AEC 1533 (approved project period commencing 11 January 2016) and AEC 1929 (approved on 10 December 2019; approved project period commencing 6 January 2020). All procedures were conducted in accordance with the Australian Code for the Care and Use of Animals for Scientific Purposes.

Informed Consent Statement: Not applicable.

Data Availability Statement: The original data presented in this study are openly available in the RMIT Research Repository at https://doi.org/10.25439/rmt.34333131.

Conflicts of Interest: The authors declare no conflict of interest.

References

1. Vogelmeier, C.F.; Gaga, M.; Aalamian−Mattheis, M.; Greulich, T.; Marin, J.M.; Castellani, W.; Ninane, V.; Lane, S.; Nunez, X.; Patalano, F.; et al. Efficacy and safety of direct switch to indacaterol/glycopyrronium in patients with moderate COPD: The CRYSTAL open−label randomised trial. *Respir. Res.* **2017**, *18*, 140. https://doi.org/10.1186/s12931−017−0622−x.
2. Barnes, P.J. Inflammatory endotypes in COPD. *Allergy* **2019**, *74*, 1249–1256. https://doi.org/10.1111/all.13760.
3. Barreiro, E.; Jaitovich, A. Muscle atrophy in chronic obstructive pulmonary disease: Molecular basis and potential therapeutic targets. *J. Thorac. Dis.* **2018**, *10*, S1415–S1424. https://doi.org/10.21037/jtd.2018.04.168.

4. Gosker, H.R.; Langen, R.C.; Simons, S.O. Role of acute exacerbations in skeletal muscle impairment in COPD. *Expert Rev. Respir. Med.* **2021**, *15*, 103–115. https://doi.org/10.1080/17476348.2021.1843429.
5. Kim, S.H.; Shin, M.J.; Shin, Y.B.; Kim, K.U. Sarcopenia Associated with Chronic Obstructive Pulmonary Disease. *J. Bone Metab.* **2019**, *26*, 65–74. https://doi.org/10.11005/jbm.2019.26.2.65.
6. Mou, K.; Chan, S.M.H.; Brassington, K.; Dobric, A.; De Luca, S.N.; Seow, H.J.; Selemidis, S.; Bozinovski, S.; Vlahos, R. Influenza A Virus−Driven Airway Inflammation may be Dissociated From Limb Muscle Atrophy in Cigarette Smoke−Exposed Mice. *Front Pharmacol.* **2022**, *13*, 859146. https://doi.org/10.3389/fphar.2022.859146.
7. Gosker, H.R.; Wouters, E.F.; van der Vusse, G.J.; Schols, A.M. Skeletal muscle dysfunction in chronic obstructive pulmonary disease and chronic heart failure: Underlying mechanisms and therapy perspectives. *Am. J. Clin. Nutr.* **2000**, *71*, 1033–1047. https://doi.org/10.1093/ajcn/71.5.1033.
8. Jaitovich, A.; Barreiro, E. Skeletal Muscle Dysfunction in Chronic Obstructive Pulmonary Disease What We Know and Can Do for Our Patients. *Am. J. Respir. Crit. Care Med.* **2018**, *198*, 175–186. https://doi.org/10.1164/rccm.201710−2140CI.
9. Zhang, L.; Sun, Y. Muscle−Bone Crosstalk in Chronic Obstructive Pulmonary Disease. *Front Endocrinol.* **2021**, *12*, 724911. https://doi.org/10.3389/fendo.2021.724911.
10. Mou, K.; Chan, S.M.H.; Vlahos, R. Musculoskeletal crosstalk in chronic obstructive pulmonary disease and comorbidities: Emerging roles and therapeutic potentials. *Pharmacol. Ther.* **2024**, *257*, 108635. https://doi.org/10.1016/j.pharmthera.2024.108635.
11. Cazzola, M.; Bajpai, J.; Calzetta, L.; Matera, M.G.; Rogliani, P. GOLD 2026: Transforming COPD Management with Early Intervention, Multi−dimensional Assessment, and Personalized Care. *Drugs* **2026**, *86*, 581–597. https://doi.org/10.1007/s40265−026−02303−3.
12. Dimopoulos, G.; Lerikou, M.; Tsiodras, S.; Chranioti, A.; Perros, E.; Anagnostopoulou, U.; Armaganidis, A.; Karakitsos, P. Viral epidemiology of acute exacerbations of chronic obstructive pulmonary disease. *Pulm. Pharmacol. Ther.* **2012**, *25*, 12–18. https://doi.org/10.1016/j.pupt.2011.08.004.
13. Kefala, A.M.; Fortescue, R.; Alimani, G.S.; Kanavidis, P.; McDonnell, M.J.; Magiorkinis, E.; Megremis, S.; Paraskevis, D.; Voyiatzaki, C.; Mathioudakis, G.A.; et al. Prevalence and clinical implications of respiratory viruses in stable chronic obstructive pulmonary disease (COPD) and exacerbations: A systematic review and meta−analysis protocol. *BMJ Open* **2020**, *10*, e035640. https://doi.org/10.1136/bmjopen−2019−035640.
14. Chen, C.Y.J.; Yew, M.S.; Abisheganaden, J.A.; Xu, H. Predictors of Influenza PCR Positivity in Acute Exacerbations of Chronic Obstructive Pulmonary Disease. *Int. J. Chron. Obstruct Pulmon Dis.* **2022**, *17*, 25–32. https://doi.org/10.2147/COPD.S338757.
15. Gosker, H.R.; Zeegers, M.P.; Wouters, E.F.M.; Schols, A.M.W.J. Muscle fibre type shifting in the vastus lateralis of patients with COPD is associated with disease severity: A systematic review and meta−analysis. *Thorax* **2007**, *62*, 944–949. https://doi.org/10.1136/thx.2007.078980.
16. Barnes, P.J. Oxidative Stress in Chronic Obstructive Pulmonary Disease. *Antioxidants* **2022**, *11*, 965. https://doi.org/10.3390/antiox11050965.
17. Chan, S.M.H.; Selemidis, S.; Vlahos, R. The Double−Edged Sword of ROS in Muscle Wasting and COPD: Insights from Aging−Related Sarcopenia. *Antioxidants* **2024**, *13*, 882. https://doi.org/10.3390/antiox13070882.
18. Galliera, E.; Massaccesi, L.; Logoluso, N.; Mangiavini, L.; Peretti, G.; Corsi Romanelli, M.M. Bone and Infections: An Osteoimmunological Interplay. *Int. J. Mol. Sci.* **2026**, *27*, 2602. https://doi.org/10.3390/ijms27062602.
19. Caetano, C.C.S.; Azamor, T.; Meyer, N.M.; Onwubueke, C.; Calabrese, C.M.; Calabrese, L.H.; Visperas, A.; Piuzzi, N.S.; Husni, M.E.; Foo, S.S.; et al. Mechanistic insights into bone remodelling dysregulation by human viral pathogens. *Nat. Microbiol.* **2024**, *9*, 322–335. https://doi.org/10.1038/s41564−023−01586−6.
20. Haudenschild, A.K.; Christiansen, B.A.; Orr, S.; Ball, E.E.; Weiss, C.M.; Liu, H.; Fyhrie, D.P.; Yik, J.H.N.; Coffey, L.L.; Haudenschild, D.R. Acute bone loss following SARS−CoV−2 infection in mice. *J. Orthop. Res.* **2023**, *41*, 1945–1952. https://doi.org/10.1002/jor.25537.
21. Reis, J.; Ramos, A. In Sickness and in Health: The Oxygen Reactive Species and the Bone. *Front Bioeng. Biotechnol.* **2021**, *9*, 745911. https://doi.org/10.3389/fbioe.2021.745911.
22. Brassington, K.; Chan, S.M.H.; De Luca, S.N.; Dobric, A.; Almerdasi, S.A.; Mou, K.; Seow, H.J.; Oseghale, O.; Bozinovski, S.; Selemidis, S.; et al. Ebselen abolishes vascular dysfunction in influenza A virus−induced exacerbations of cigarette smoke−induced lung inflammation in mice. *Clin. Sci.* **2022**, *136*, 537–555. https://doi.org/10.1042/CS20211090.
23. Brassington, K.; Chan, S.M.H.; Seow, H.J.; Dobric, A.; Bozinovski, S.; Selemidis, S.; Vlahos, R. Ebselen reduces cigarette smoke−induced endothelial dysfunction in mice. *Br. J. Pharmacol.* **2021**, *178*, 1805–1818. https://doi.org/10.1111/bph.15400.

24. Fermoselle, C.; Rabinovich, R.; Ausin, P.; Puig−Vilanova, E.; Coronell, C.; Sanchez, F.; Roca, J.; Gea, J.; Barreiro, E. Does oxidative stress modulate limb muscle atrophy in severe COPD patients? *Eur. Respir. J.* **2012**, *40*, 851–862. https://doi.org/10.1183/09031936.00137211.
25. Gea, J.; Orozco−Levi, M.; Pascual−Guardia, S.; Casadevall, C.; Enriquez−Rodriguez, C.J.; Camps−Ubach, R.; Barreiro, E. Biological Mechanisms Involved in Muscle Dysfunction in COPD: An Integrative Damage−Regeneration−Remodeling Framework. *Cells* **2025**, *14*, 1731. https://doi.org/10.3390/cells14211731.
26. Chan, S.M.H.; Bernardo, I.; Mastronardo, C.; Mou, K.; De Luca, S.N.; Seow, H.J.; Dobric, A.; Brassington, K.; Selemidis, S.; Bozinovski, S.; et al. Apocynin prevents cigarette smoking−induced loss of skeletal muscle mass and function in mice by preserving proteostatic signalling. *Br. J. Pharmacol.* **2021**, *178*, 3049–3066. https://doi.org/10.1111/bph.15482.
27. Wald, N.; Idle, M.; Bailey, A. Carboxyhaemoglobin levels and inhaling habits in cigarette smokers. *Thorax* **1978**, *33*, 201–206. https://doi.org/10.1136/thx.33.2.201.
28. Braun, M.; Koger, F.; Klingelhöfer, D.; Müller, R.; Groneberg, D.A. Particulate Matter Emissions of Four Different Cigarette Types of One Popular Brand: Influence of Tobacco Strength and Additives. *Int. J. Env. Res. Public Health* **2019**, *16*, 263. https://doi.org/10.3390/ijerph16020263.
29. Chan, S.M.H.; Brassington, K.; Almerdasi, S.A.; Dobric, A.; De Luca, S.N.; Coward−Smith, M.; Wang, H.; Mou, K.; Akhtar, A.; Alateeq, R.A.; et al. Inhibition of oxidative stress by apocynin attenuated chronic obstructive pulmonary disease progression and vascular injury by cigarette smoke exposure. *Br. J. Pharmacol.* **2023**, *180*, 2018–2034. https://doi.org/10.1111/bph.16068.
30. Campbell, G.M.; Sophocleous, A. Quantitative analysis of bone and soft tissue by micro−computed tomography: Applications to ex vivo and in vivo studies. *Bonekey Rep.* **2014**, *3*, 564. https://doi.org/10.1038/bonekey.2014.59.
31. Chan, S.M.H.; Cerni, C.; Passey, S.; Seow, H.J.; Bernardo, I.; van der Poel, C.; Dobric, A.; Brassington, K.; Selemidis, S.; Bozinovski, S.; et al. Cigarette Smoking Exacerbates Skeletal Muscle Injury without Compromising Its Regenerative Capacity. *Am. J. Respir. Cell Mol. Biol.* **2020**, *62*, 217–230. https://doi.org/10.1165/rcmb.2019−0106OC.
32. Roux, C.; Briot, K. Current role for bone absorptiometry. *Jt. Bone Spine* **2017**, *84*, 35–37. https://doi.org/10.1016/j.jbspin.2016.02.032.
33. Malaval, L.; Wade−Gueye, N.M.; Boudiffa, M.; Fei, J.; Zirngibl, R.; Chen, F.; Laroche, N.; Roux, J.P.; Burt−Pichat, B.; Duboeuf, F.; et al. Bone sialoprotein plays a functional role in bone formation and osteoclastogenesis. *J. Exp. Med.* **2008**, *205*, 1145–1153. https://doi.org/10.1084/jem.20071294.
34. Ma, R.; Su, Y.; Cao, R.; Wang, K.; Yang, P. Enhanced Osteogenic Activity and Bone Repair Ability of PLGA/MBG Scaffolds Doped with ZIF−8 Nanoparticles Loaded with BMP−2. *Int. J. Nanomed.* **2023**, *18*, 5055–5072. https://doi.org/10.2147/IJN.S423985.
35. Ding, W.; Lv, D.; Wang, M.; Pei, D. IBSP Promotes Breast Cancer Bone Metastasis and Proliferation via BMP−SMAD Signaling Pathway. *Cancer Rep.* **2024**, *7*, e2153. https://doi.org/10.1002/cnr2.2153.
36. Maltby, S.; Lochrin, A.J.; Bartlett, B.; Tay, H.L.; Weaver, J.; Poulton, I.J.; Plank, M.W.; Rosenberg, H.F.; Sims, N.A.; Foster, P.S. Osteoblasts Are Rapidly Ablated by Virus−Induced Systemic Inflammation following Lymphocytic Choriomeningitis Virus or Pneumonia Virus of Mice Infection in Mice. *J. Immunol.* **2018**, *200*, 632–642. https://doi.org/10.4049/jimmunol.1700927.
37. Braunstein, I.; Motohashi, H.; Dallenga, T.; Schaible, U.E.; Benhar, M. Redox signaling in innate immunity and inflammation: Focus on macrophages and neutrophils. *Free Radic. Biol. Med.* **2025**, *237*, 427–454. https://doi.org/10.1016/j.freeradbiomed.2025.06.006.
38. Kombe Kombe, A.J.; Fotoohabadi, L.; Gerasimova, Y.; Nanduri, R.; Lama Tamang, P.; Kandala, M.; Kelesidis, T. The Role of Inflammation in the Pathogenesis of Viral Respiratory Infections. *Microorganisms* **2024**, *12*, 2526. https://doi.org/10.3390/microorganisms12122526.
39. Zhang, J.; Luo, W.; Miao, C.; Zhong, J. Hypercatabolism and Anti−catabolic Therapies in the Persistent Inflammation, Immunosuppression, and Catabolism Syndrome. *Front. Nutr.* **2022**, *9*, 941097. https://doi.org/10.3389/fnut.2022.941097.
40. Ji, Y.; Li, M.; Chang, M.; Liu, R.; Qiu, J.; Wang, K.; Deng, C.; Shen, Y.; Zhu, J.; Wang, W.; et al. Inflammation: Roles in Skeletal Muscle Atrophy. *Antioxidants* **2022**, *11*, 1686. https://doi.org/10.3390/antiox11091686.
41. Crupi, A.N.; Nunnelee, J.S.; Taylor, D.J.; Thomas, A.; Vit, J.P.; Riera, C.E.; Gottlieb, R.A.; Goodridge, H.S. Oxidative muscles have better mitochondrial homeostasis than glycolytic muscles throughout life and maintain mitochondrial function during aging. *Aging* **2018**, *10*, 3327–3352. https://doi.org/10.18632/aging.101643.
42. Corrà, S.; Young, L.; Moore, A.L.; Viscomi, C. Mitochondrial disease: Mechanisms, signalling, and therapeutic opportunities. *Free Radic. Bio Med.* **2026**, *253*, 749–769. https://doi.org/10.1016/j.freeradbiomed.2026.06.013.
43. Supruniuk, E.; Gorski, J.; Chabowski, A. Endogenous and Exogenous Antioxidants in Skeletal Muscle Fatigue Development during Exercise. *Antioxidants* **2023**, *12*, 501. https://doi.org/10.3390/antiox12020501.

44. Zhuang, Z.; Meng, Y.; Xue, Y.; Wang, Y.; Cheng, X.; Jing, J. Adaptation of STIM1 structure−function relationships for optogenetic control of calcium signaling. *J. Biol. Chem.* **2024**, *300*, 107636. https://doi.org/10.1016/j.jbc.2024.107636.
45. Li, X.; Zhao, X.; Qin, Z.; Li, J.; Sun, B.; Liu, L. Regulation of calcium homeostasis in endoplasmic reticulum−mitochondria crosstalk: Implications for skeletal muscle atrophy. *Cell Commun. Signal* **2025**, *23*, 17. https://doi.org/10.1186/s12964−024−02014−w.
46. Wilson, R.J.; Lyons, S.P.; Koves, T.R.; Bryson, V.G.; Zhang, H.; Li, T.; Crown, S.B.; Ding, J.D.; Grimsrud, P.A.; Rosenberg, P.B.; et al. Disruption of STIM1−mediated Ca^{2+} sensing and energy metabolism in adult skeletal muscle compromises exercise tolerance, proteostasis, and lean mass. *Mol. Metab.* **2022**, *57*, 101429. https://doi.org/10.1016/j.molmet.2021.101429.
47. Qaisar, R.; Bhaskaran, S.; Premkumar, P.; Ranjit, R.; Natarajan, K.S.; Ahn, B.; Riddle, K.; Claflin, D.R.; Richardson, A.; Brooks, S.V.; et al. Oxidative stress−induced dysregulation of excitation−contraction coupling contributes to muscle weakness. *J. Cachexia Sarcopenia Muscle* **2018**, *9*, 1003–1017. https://doi.org/10.1002/jcsm.12339.
48. Lian, D.; Chen, M.M.; Wu, H.; Deng, S.; Hu, X. The Role of Oxidative Stress in Skeletal Muscle Myogenesis and Muscle Disease. *Antioxidants* **2022**, *11*, 755. https://doi.org/10.3390/antiox11040755.
49. Spruit, M.A.; Gosselink, R.; Troosters, T.; Kasran, A.; Gayan−Ramirez, G.; Bogaerts, P.; Bouillon, R.; Decramer, M. Muscle force during an acute exacerbation in hospitalised patients with COPD and its relationship with CXCL8 and IGF−I. *Thorax* **2003**, *58*, 752–756. https://doi.org/10.1136/thorax.58.9.752.
50. Powers, S.K.; Schrager, M. Redox signaling regulates skeletal muscle remodeling in response to exercise and prolonged inactivity. *Redox Biol.* **2022**, *54*, 102374. https://doi.org/10.1016/j.redox.2022.102374.
51. Gea, J.; Sancho−Munoz, A.; Chalela, R. Nutritional status and muscle dysfunction in chronic respiratory diseases: Stable phase versus acute exacerbations. *J. Thorac. Dis.* **2018**, *10*, S1332–S1354. https://doi.org/10.21037/jtd.2018.02.66.
52. Bhatt, S.P.; Agusti, A.; Bafadhel, M.; Christenson, S.A.; Bon, J.; Donaldson, G.C.; Sin, D.D.; Wedzicha, J.A.; Martinez, F.J. Phenotypes, Etiotypes, and Endotypes of Exacerbations of Chronic Obstructive Pulmonary Disease. *Am. J. Respir. Crit. Care Med.* **2023**, *208*, 1026–1041. https://doi.org/10.1164/rccm.202209−1748SO.
53. Duong, M.L.; Qian, C.; Talukdar, M.; Kayaniyil, S.; Karissa, J.; Nordon, C.; Penz, E.D. Frequency and severity of COPD exacerbations and future risk of exacerbations and mortality: An observational cohort study in Canada. *BMJ Open Respir. Res.* **2025**, *12*, e002976. https://doi.org/10.1136/bmjresp−2024−002976.
54. Hurst, J.R.; Skolnik, N.; Hansen, G.J.; Anzueto, A.; Donaldson, G.C.; Dransfield, M.T.; Varghese, P. Understanding the impact of chronic obstructive pulmonary disease exacerbations on patient health and quality of life. *Eur. J. Intern Med.* **2020**, *73*, 1–6. https://doi.org/10.1016/j.ejim.2019.12.014.

Disclaimer/Publisher's Note: The statements, opinions and data contained in all publications are solely those of the individual author(s) and contributor(s) and not of MDPI and/or the editor(s). MDPI and/or the editor(s) disclaim responsibility for any injury to people or property resulting from any ideas, methods, instructions or products referred to in the content.